Optimal control of pretwisted adaptive rotating blades modeled as anisotropic thin-walled beams with piezo-composite

Xiao Wang, Pierangelo Masarati
Dipartimento di Scienze e Tecnologie Aerospaziali, Politecnico di Milano, Italy

Abstract

Problems related to mathematical modeling and optimal dynamic control of pretwisted adaptive rotating blade are considered. The blade is modeled as a thin-walled beam accounting for nonclassical effects, such as anisotropy, transverse shear and warping inhibitions. The adaptive capabilities are provided by the actuators manufactured by anisotropic piezo-composite layers embedded into the structure. The linear quadratic regulator feedback control strategy is adopted to study the dynamic behavior on vibration suppression. The control authority of the implementation of piezo-actuators with different ply-angles, considered in conjunction with that of the structural tailoring, are highlighted.

1 Introduction

Because of the advantages with respect to weight criteria, specific high stiffness and elastic couplings, composite thin-walled structures are widely used in the rotor blade structure design. A large amount of work are devoted to the modeling and behavior of composite rotor blades [1;2;3;4;5;6;7;8;9;10;11]. Recently, the blade incorporating adaptive materials technology into the host structure are proposed for the design of new high performing blades [12;13;14;15]. In contrast to the passive control via tailoring technology, in those featuring adaptive capabilities, the frequencies, mode shapes and damping can be tuned to avoid structural resonance and to enhance dynamic response characteristics. Because piezoelectric materials have a series of desirable characteristics, such as self-sensing, fast response and covering a broad range of frequency, they are excellent candidates for the role of sensors and actuators.

In the existing literature, a lot publications on modeling or studying adaptive thin-walled structure are based on the assumption of fiber orientation of piezo-composite are aligned along the spanwise missing the discussion of the isotropic properties [16;17;18;19;20;21;22]. Thus the system can only be controlled by the piezoelectrically induced bending moments. Wang et al. develop a geometrically nonlinear thin-walled beam theory incorporating fiber-reinforced composite and piezo-composite in Ref. [23;24] and give a comprehensive study allowing to get a better insight into the influence of piezoelectrically induced extension, transverse shear, twist, bimoment and bending actuations.

In this paper, based on the pretwisted adaptive rotating blade model developed in Ref. [24], the control authority on vibration suppression is investigated when implementing the Linear Quadratic Regular (LQR) optimal control strategy. The Extended Galerkin's Method (EGM) is used to semi-discretize the governing equation of the system for numerical study. The influence of ply-angles of host structure and piezo-actuator are highlighted.

2 Basic assumptions and kinematics

2.1 Basic assumptions

A pretwisted rotary thin-walled beam incorporating fiber-reinforced composite and piezo-composite materials is considered in the present article. The geometric configuration and the chosen coordinate systems are shown in Figs 1 and 2.

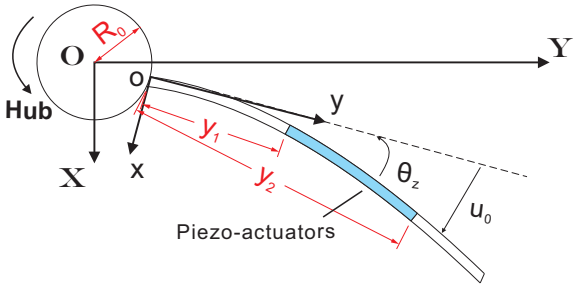

Figure 1: A schematic description of the blade.

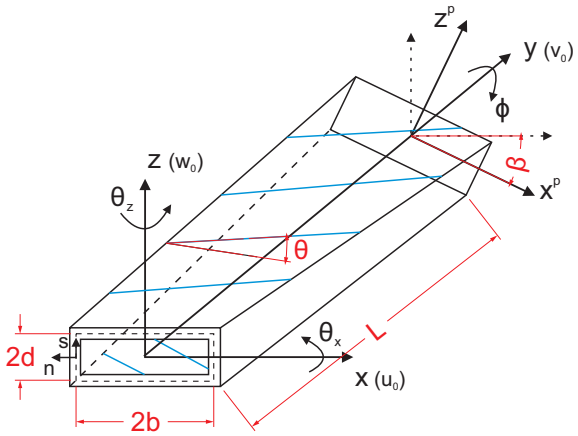

Figure 2: Geometry of the pretwisted beam with a rectangular cross-section (CUS lay-ups).

The inertial reference system (X,Y,Z) is attached to the center of the hub O (considered to be rigid), while the rotating axis system (x,y,z) is located at the blade root with an offset R_0 from the rotation axis O, see Fig. 1. The unit vectors associated with the frame coordinates (X,Y,Z) and (x,y,z) are defined as $(\mathbf{I},\mathbf{J},\mathbf{K})$ and $(\mathbf{i},\mathbf{j},\mathbf{k})$, respectively. Besides the rotating coordinate system (x,y,z), a local coordinate system (x^p,y,z^p) is also defined, where x^p and z^p are the principal axes of an arbitrary beam cross-section, see Fig. 2. In addition, a surface coordinate system (s,y,n) on the mid-line contour of the cross-section is considered in Fig. 2. Coordinate systems (x,y,z) and (x^p,y,z^p) are related by the following transformation

$$\begin{cases} x(s,y) = x^p(s)\cos\beta(y) + z^p(s)\sin\beta(y), \\ z(s,y) = -x^p(s)\sin\beta(y) + z^p(s)\cos\beta(y), \end{cases} \tag{1}$$

where the linear pretwist angle $\beta(y)$ can be assumed as

$$\beta(y) = \gamma_0 + \beta_0\frac{y}{L}, \tag{2}$$

in which γ_0, β_0 and L denote the presetting angle, the pretwist angle of the cross-section at the beam tip and the length of the beam, respectively.

Toward the modeling of the rotary thin-walled structure, the same assumptions used in Ref.[25] are adopted, such as (i) the cross-section is assumed preserved during the deformation; (ii) both the primary and secondary (thickness) warping effects are included; (iii) the transverse shear effect are taken into account. Note that, the centrifugal stiffening and tennis-racket effects[26] are highlighted in the present approach.

2.2 Kinematics

It is useful to express the position vector $\mathbf{R}$ of an arbitrary point $M(x,y,z)$ belonging to the deformed beam, measured from a fixed origin O (coinciding with the center of the hub), described in the rotating coordinate system (x,y,z). In the sense we have

$$\mathbf{R} = \mathbf{R}_0 + \mathbf{r} + \mathbf{D}, \tag{3}$$

where $\mathbf{R}_0$, $\mathbf{r}$ and $\mathbf{D}$ denote the position vector of the beam root point o (hub periphery), the undeformed position vector of point $M(x,y,z)$, and its displacement vector, respectively. Their expressions are

$$\mathbf{R}_0 = R_0\mathbf{j}, \quad \mathbf{r} = x\mathbf{i} + y\mathbf{j} + z\mathbf{k}, \quad \mathbf{D} = u\mathbf{i} + v\mathbf{i} + w\mathbf{k}, \tag{4}$$

where the components u, v and w in the displacement vector $\mathbf{D}$ are[25]

$$\begin{aligned} u(x,y,z,t) =& u_0(x,t) + \left[z(s) + n\frac{\mathrm{d}x}{\mathrm{d}s}\right]\sin\phi(y,t) \\ &- \left[x(s) - n\frac{\mathrm{d}z}{\mathrm{d}s}\right][1-\cos\phi(y,t)], \end{aligned} \tag{5a}$$

$$\begin{aligned} v(x,y,z,t) =& v_0(y,t) + \left[x(s) - n\frac{\mathrm{d}z}{\mathrm{d}s}\right]\theta_z(y,t) \\ &+ \left[z(s) + n\frac{\mathrm{d}x}{\mathrm{d}s}\right]\theta_x(y,t) - [F_w(s) + na(s)]\phi'(y,t), \end{aligned} \tag{5b}$$

$$\begin{aligned} w(x,y,z,t) =& w_0(y,t) - \left[x(s) - n\frac{\mathrm{d}z}{\mathrm{d}s}\right]\sin\phi(y,t) \\ &- \left[z(s) + n\frac{\mathrm{d}x}{\mathrm{d}s}\right][1-\cos\phi(y,t)], \end{aligned} \tag{5c}$$

where $F_w(s)$ and $na(s)$ play the role of primary and secondary warping functions. $u_0(y,t)$, $v_0(y,t)$, $w_0(y,t)$, $\phi(y,t)$, $\theta_x(y,t)$, $\theta_z(y,t)$ represent the 1-D displacement measures (see Fig. 2), and constitute the basic unknowns of the problem. If we assume that the rotation takes place in the plane (X,Y) with the constant angular speed, i.e., $\Omega = \Omega\mathbf{K} = \Omega\mathbf{k}$, the velocity and acceleration vectors of point $M(x,y,z)$ can be given as:

$$\begin{aligned} \dot{\mathbf{R}}(x,y,z) =& \dot{u}(x,y,z)\mathbf{i} - [R_0 + y + v(x,y,z)]\Omega\mathbf{i} + \dot{v}(x,y,z)\mathbf{j} \\ &+ [x + u(x,y,z)]\Omega\mathbf{j} + \dot{w}\mathbf{k}, \end{aligned} \tag{6}$$

$$\begin{aligned} \ddot{\mathbf{R}}(x,y,z) =& \ddot{u}(x,y,z)\mathbf{i} - 2\dot{v}(x,y,z)\Omega\mathbf{i} - [x + u(x,y,z)]\Omega^2\mathbf{i} + \ddot{v}(x,y,z)\mathbf{j} \\ &+ 2\dot{u}(x,y,z)\Omega - [R_0 + y + v(x,y,z)]\Omega^2\mathbf{j} + \ddot{w}\mathbf{k}. \end{aligned} \tag{7}$$

2.3 Strains

The strains that contribute to the potential energy are: Spanwise strain:

$$\varepsilon_{yy}(n,s,y,t) = \varepsilon^0_{yy}(s,y,t) + n\varepsilon^1_{yy}(s,y,t), \tag{8}$$

where ε^0_{yy} denotes the axial strain associated with the primary warping and ε^1_{yy} denotes a measure of curvature associated with the secondary warping, their explicit expressions are given as

$$\begin{aligned} \varepsilon^0_{yy} =& \left[v_0' + x\theta_z' + z\theta_x' - F_w\phi''\right] + \frac{1}{2}\left[(u_0')^2 + (w_0')^2 + (x^2+z^2)\phi'^2\right] \\ &+ u_0'\phi'(z\cos\phi - x\sin\phi) - w_0'\phi'(x\cos\phi + z\sin\phi), \end{aligned} \tag{9a}$$

$$\begin{aligned} \varepsilon^1_{yy} =& -\frac{\mathrm{d}z}{\mathrm{d}s}\theta_z' + \frac{\mathrm{d}x}{\mathrm{d}s}\theta_x' - a\phi'' \\ &+ \phi'\left[u_0'\left(\frac{\mathrm{d}x}{\mathrm{d}s}\cos\phi + \frac{\mathrm{d}z}{\mathrm{d}s}\sin\phi\right) + w_0'\left(\frac{\mathrm{d}z}{\mathrm{d}s}\cos\phi - \frac{\mathrm{d}x}{\mathrm{d}s}\sin\phi\right) + r_n\phi'\right]. \end{aligned} \tag{9b}$$

Tangential shear strain:

$$\gamma_{sy}(s,y,t) = \gamma^0_{sy}(s,y,t) + \Psi(s)\phi'(y,t) + 2n\phi', \tag{10}$$

where

$$\gamma^0_{sy} = \frac{\mathrm{d}x}{\mathrm{d}s}(\theta_z + u_0'\cos\phi - w_0'\sin\phi) + \frac{\mathrm{d}z}{\mathrm{d}s}(\theta_x + u_0'\sin\phi + w_0'\cos\phi). \tag{11}$$

Transverse shear stain:

$$\gamma_{ny} = \frac{\mathrm{d}x}{\mathrm{d}s}(\theta_x + u_0' \in \phi + w_0'\cos\phi) - \frac{\mathrm{d}z}{\mathrm{d}s}(\theta_z + u_0'\cos\phi - w_0'\sin\phi). \tag{12}$$

3 Constitutive Relations

The fiber-reinforced composite material (e.g. Graphite-Epoxy) in host structure and the piezo-composite material (e.g. AFC[27] or MFC[28]) in actuator can both be modeled using the linear piezoelectric constitutive equation[24;25]. The stress resultants and stress couples reduce to the following expressions

(13)
$$\begin{Bmatrix} N_{yy} \\ N_{ys} \\ L_{yy} \\ L_{sy} \end{Bmatrix} = \begin{bmatrix} K_{11} & K_{12} & K_{13} & K_{14} \\ K_{21} & K_{22} & K_{23} & K_{24} \\ K_{41} & K_{42} & K_{43} & K_{44} \\ K_{51} & K_{52} & K_{53} & K_{54} \end{bmatrix} \begin{Bmatrix} \varepsilon^0_{yy} \\ \gamma^0_{ys} \\ \phi' \\ \varepsilon^1_{yy} \end{Bmatrix} - \begin{Bmatrix} \tilde{N}_{yy} \\ \tilde{N}_{sy} \\ \tilde{L}_{yy} \\ \tilde{L}_{sy} \end{Bmatrix},$$

and

(14)
$$N_{yn} = \left(A_{44} - \frac{{A_{45}}^2}{A_{55}} \right) \gamma_{yn}.$$

The explicit expressions of the local stiffness coefficients K_{ij} and piezoelectrically induced resultants (e.g., $\tilde{N}_{yy}$) are given in Ref.[25] and[23], respectively.

4 Formulation of the governing system

The governing equations and the associated boundary conditions are derived from Hamilton's principle. This can be stated as (see e.g. Ref.[25])

(15)
$$\int_{t_0}^{t_1} [\delta T + \delta V - \delta W_e] \, \mathrm{d}t = 0,$$

where the virtual work of the external excitation W_e, the kinetic energy T and strain energy V can be given as

(16a)
$$T = \frac{1}{2} \int_0^L \oint_c \sum_{k=1}^{N_{hp}} \int_{n_{k1}}^{n_{k2}} \rho(k) (\dot{\mathbf{R}} \cdot \dot{\mathbf{R}}) \, \mathrm{d}n \, \mathrm{d}s \, \mathrm{d}y,$$

(16b)
$$V = \frac{1}{2} \int_0^L \oint_c \left[N_{yy}\varepsilon^0_{yy} + N_{ys}\gamma^0_{sy} + L_{yy}\varepsilon^1_{yy} + L_{sy}\phi' + N_{ny}\gamma_{ny} \right] \mathrm{d}s \, \mathrm{d}y,$$

(16c)
$$W_e = \int_0^L \Big[p_x u_0 + p_y v_0 + p_z w_0 + m_x \theta_x + (m_y + b_w{}')\phi + m_z \theta_z \Big] \, \mathrm{d}y,$$

In Eqs. (15) and (16), t_0 and t_1 denote two arbitrary motions of time; ρ denotes the mass density; p_x, p_y, p_z, m_x, m_y, m_z and b_w are the external excitation per unit span length; while δ, $\dot{()}$ and $()'$ denote the variation operator, $\partial()/\partial t$ and $\partial()/\partial y$, respectively.

The governing system of the pretwisted rotating blades will be expressed in terms of displacement quantitites. For the general case of ply-up configuration, the system exhibits a complete coupling between the various modes, that is, warping (primary and secondary), bending (flapping and lagging), transverse shearing, twist and extension. In engineering applications, special lay-up configuration is normally adopted to design particular couplings[29]. Here, *circumferentially uniform stiffness* (CUS) configuration[30] is considered. For the thin-walled beam with rectangular cross-section as shown in Fig. 2, CUS configuration implies the ply-angle distribution $\theta(z) = \theta(-z)$ of the top and bottom walls and $\theta(x) = \theta(-x)$ of the left and right walls. Indicated in Ref.[24], CUS configuration will decouple the system into two independent subsystems, i.e., one governs the flapwise bending-chordwise bending coupling motion and the other governs the twist-extension coupling motion. Since the inclusion of pretwist solely has the significant effect on the former subsystem, this article is focused on this one.

After a lengthy variation process of Eq. 15 and ignoring the immaterial nonlinear terms, the governing equations expressed in terms of displacement quantities as

(17a)
$$\begin{aligned} \delta u_0 : {} & a_{34}\theta_x'' + a_{44}(u_0'' + \theta_z') + p_x + \underline{b_1 \Omega^2 [R(y) u_0']'} \\ & - b_1 [\ddot{u}_0 - \underbrace{2\Omega \dot{v}_0} - \underline{\Omega^2 u_0}] + \delta_p \mathcal{A}_1^{Qx} V_1 P'(y) = 0, \end{aligned}$$

(17b)
$$\begin{aligned} \delta w_0 : {} & a_{25}\theta_z'' + a_{55}(w_0'' + \theta_x') + \underline{b_1 \Omega^2 [R(y) w_0']'} - b_1 \ddot{w}_0 + p_z \\ & + \delta_p \mathcal{A}_3^{Qz} V_3 P'(y) = 0, \end{aligned}$$

(17c)
$$\begin{aligned} \delta\theta_x : {} & a_{33}\theta_x'' + a_{34}(u_0'' + \theta_z') - a_{25}\theta_z' - a_{55}(w_0' + \theta_x) \\ & + m_x - b_4 \ddot{\theta}_x - b_6 \ddot{\theta}_z - \underbrace{2\Omega b_4 \dot{\phi}} \\ & + \underline{\underline{\Omega^2 (b_4 \theta_x + b_6 \theta_z)}} + \delta_p \mathcal{A}_1^{Mx} V_1 P'(y) - \mathcal{A}_3^{Qz} V_3 P(y) = 0, \end{aligned}$$

(17d)
$$\begin{aligned} \delta\theta_z : {} & a_{22}\theta_z'' + a_{25}(w_0'' + \theta_x') - a_{34}\theta_x' - a_{44}(u_0' + \theta_z) \\ & + m_z - b_5 \ddot{\theta}_z - b_6 \ddot{\theta}_x - \underbrace{2\Omega b_6 \dot{\phi}} + \underline{\underline{\Omega^2 (b_5 \theta_z + b_6 \theta_x)}} \\ & + \delta_p \mathcal{A}_3^{Mz} V_3 P'(y) - \mathcal{A}_1^{Qx} V_1 P(y) = 0, \end{aligned}$$

the boundary conditions are
at $y = 0$:

(18)
$$u_0 = w_0 = \theta_x = \theta_z = 0,$$

and at $y = L$:

(19a)
$$\begin{aligned} \delta u_0 : {} & a_{24}(L)\theta_z' + a_{34}(L)\theta_x' + a_{44}(L)(u_0' + \theta_z) + a_{45}(L)(w_0' + \theta_x) \\ & + \delta_s \left[\mathcal{A}_1^{Qx} V_1 \cos\beta(L) + \mathcal{A}_3^{Qz} V_3 \sin\beta(L) \right] = 0, \end{aligned}$$

(19b)
$$\begin{aligned} \delta w_0 : {} & a_{25}(L)\theta_z' + a_{35}(L)\theta_x' + a_{45}(L)(u_0' + \theta_z) + a_{55}(L)(w_0' + \theta_x) \\ & + \delta_s \left[\mathcal{A}_3^{Qz} V_3 \cos\beta(L) - \mathcal{A}_1^{Qx} V_1 \sin\beta(L) \right] = 0, \end{aligned}$$

(19c)
$$\begin{aligned} \delta\theta_x : {} & a_{23}(L)\theta_z' + a_{33}(L)\theta_x' + a_{34}(L)(u_0' + \theta_z) + a_{35}(L)(w_0' + \theta_x) \\ & + \delta_s \left[\mathcal{A}_1^{Mx} V_1 \cos\beta(L) - \mathcal{A}_3^{Mz} V_3 \sin\beta(L) \right] = 0, \end{aligned}$$

(19d)
$$\begin{aligned} \delta\theta_z : {} & a_{22}(L)\theta_z' + a_{23}(L)\theta_x' + a_{24}(L)(u_0' + \theta_z) + a_{25}(L)(w_0' + \theta_x) \\ & + \delta_s \left[\mathcal{A}_3^{Mz} V_3 \cos\beta(L) + \mathcal{A}_1^{Mx} V_1 \sin\beta(L) \right] = 0, \end{aligned}$$

In these equations

$$R(y) = R_0(L-y) + \frac{1}{2}(L^2 - y^2), \tag{20}$$

$a_{ij}(y)$, $b_{ij}(y)$ and $\mathcal{A}_i^X$ are the stiffness, mass and piezo-actuator coefficients, respectively. There explicit expressions are presented in Refs.[25;23;24]. $P(y)$ denotes the span location of the piezo-actuator of Fig. 1

$$P(y) = H(y-y_1) - H(y-y_2), \tag{21}$$

$H(\cdot)$ is Heavisides distribution. The piezo-actuators can be split into two actuators pairs, see Fig. 3. The voltage parameters V_1 and V_3 are related to flange-actuator-pair (top and bottom) and web-actuator-pair (left and right), respectively.

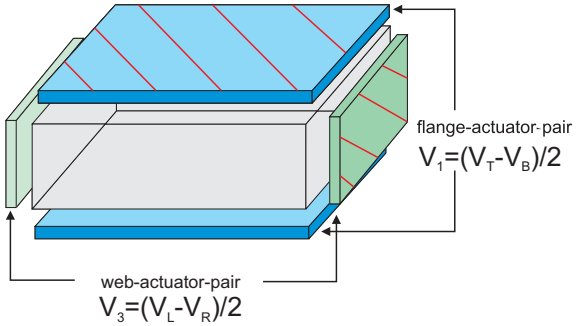

Figure 3: Rotary beam with a rectangular cross-section.

For the cases (a) the actuator is spread over the entire beam span (b) the actuator is a single patch, the traces have to be taken as (a) $\delta_p = 0$ and $\delta_s = 1$ (b) $\delta_p = 1$ and $\delta_s = 0$, respectively.

In a nutshell, the terms in Eqs. (17) associated with (1) the centrifugal acceleration, (2) the Coriolis, (3) the tennis-racket, (4) the centrifugal warping and (5) the centrifugal-rotatory effects are underscored by (1) a solid line (____), (2) a wavy line (~~~~), (3) a dotted line (. . . .), (4) a dashed line (- - - -) and (5) two superposed solid lines (=====) respectively.

5 Solution methodology

5.1 The Extend Galerkin's Method

The Extend Galerkin's Method (EGM)[31;32] is applied to discretize the system for numerical study. The underlying idea of EGM is to select weighting (or shape) functions that exactly satisfy only the geometric boundary conditions ($y = 0$). The terms arising as a result of the non-fulfillment of natural boundary conditions ($y = L$) remain as residual terms in the energy functional itself, which are then minimized in the Galerkin sense[33], thus yielding excellent accuracy and rapid convergence[32]. Let

$$\begin{aligned} u_0(y,t) &= \Psi_u^T(y)\mathbf{q}_u(t), \quad w_0(y,t) = \Psi_w^T(y)\mathbf{q}_w(t), \\ \theta_x(y,t) &= \Psi_x^T(y)\mathbf{q}_x(t), \quad \theta z(y,t) = \Psi_z^T(y)\mathbf{q}_z(t), \end{aligned} \tag{22}$$

where the shape functions $\Psi_u^T(y)$, $\Psi_w^T(y)$, $\Psi_x^T(y)$ and $\Psi_z^T(y)$ are required to fulfill the geometric boundary conditions. Thus the discretized forms of the system when ignoring the immaterial Coriolis terms follow as

$$\mathbf{M}\ddot{\mathbf{q}} + [\mathbf{K} + \Omega^2\hat{\mathbf{K}}]\mathbf{q} + \mathcal{A}_\mathbf{1}V_1 + \mathcal{A}_\mathbf{3}V_3 = \mathbf{Q}, \tag{23}$$

where

$$\mathbf{q} = \left\{\mathbf{q}_u^T \quad \mathbf{q}_w^T \quad \mathbf{q}_x^T \quad \mathbf{q}_z^T\right\}^T, \tag{24}$$

The expressions for mass matrix $\mathbf{M}$, stiffness matrix $\mathbf{K}$, dynamical stiffness matrix $\hat{\mathbf{K}}$, actuating vector $\mathcal{A}_\mathbf{i}$ and external excitation vector $\mathbf{Q}$ are given in appendix of Ref.[24].

5.2 Linear Quadratic Regulator optimal control

One important target of the piezo-actuators is to suppress the vibration of the blade. To achieve this target, linear quadratic regulator (LQR) optimal control based on the use of a full state feedback scheme is adopted. Eq. (23) can be cast in state-space form as

$$\dot{\mathbf{x}}(t) = \mathbf{A}\mathbf{x}(t) + \mathbf{B}\mathbf{Q}(t) - \mathbf{B}\mathcal{A}_\mathbf{1}V_1(t) - \mathbf{B}\mathcal{A}_\mathbf{3}V_3(t) \tag{25}$$

where,

$$\mathbf{x}(t) = \begin{bmatrix}\mathbf{q}^T(t) \\ \dot{\mathbf{q}}^T(t)\end{bmatrix}, \quad \mathbf{A} = \begin{bmatrix}\mathbf{0} & \mathbf{I} \\ -\mathbf{M}^{-1}\mathbf{K} & \mathbf{0}\end{bmatrix}, \quad \mathbf{B} = \begin{Bmatrix}\mathbf{0} \\ \mathbf{M}^{-1}\end{Bmatrix}. \tag{26}$$

Note that the LQR control provides sort of a benchmark, an ideal optimal value which cannot be obtained in practical applications because the state x is not available and needs to be reconstructed using a state estimator that degrades the quality of the regulator. Within the LQR control algorithm, we minimize the cost function (both the response of the closed-loop system and the control effort should be minimized simultaneously).

$$J = \frac{1}{2}\int_{t_0}^{t_f} \left(\mathbf{x}^T\mathbf{Z}\mathbf{x} + V_i R_i V_i\right) \mathrm{d}t, \tag{27}$$

where positive semidefinite matrix $\mathbf{Z}$ and positive definite scalar R_i denote the state weighting matrix and the control weighting scalar, respectively, while t_0 and t_f denote the present and the final time, respectively. Following Ref.[34], the weighting matrices $\mathbf{Z}$ and R_i proper to a trade off between control effectiveness and control energy consumption by taking

$$\mathbf{Z} = \begin{bmatrix}\alpha\mathbf{K} & \mathbf{0} \\ \mathbf{0} & \beta\mathbf{M}\end{bmatrix}, \quad R_i = \eta_i \mathcal{A}_\mathbf{i}^T \mathbf{K}^{-1} \mathcal{A}_\mathbf{i}, \quad (i = 1,3) \tag{28}$$

where α and β are weighting coefficients, ($\alpha\beta \geq 0$ and $(\alpha+\beta) > 0$), where η_i is a positive scale factor. The matrix $\mathbf{Z}$ actually represents the sum of the system kinetic and potential energies in the sense of

$$\frac{1}{2}\int_{t_0}^{t_f} \mathbf{x}^T\mathbf{Z}\,\mathrm{d}t = \frac{1}{2}\int_{t_0}^{t_f} \left[\dot{\mathbf{q}}^T\beta\mathbf{M}\dot{\mathbf{q}} + \mathbf{q}^T\alpha\mathbf{K}\mathbf{q}\right] \mathrm{d}t. \tag{29}$$

On the perspective of vibration suppression, it is reasonable to just consider the system kinetic energy, i.e., weighting coefficients combination $\alpha = 0$ and $\beta = 1$ is adopted in the context. Thus, the LQR optimal feedback control law can be given as

$$V_i(t) = -\mathbf{G}_i \mathbf{x}(t), \tag{30}$$

where $\mathbf{G}_i$ is the optimal gain matrix,

$$\mathbf{G}_i = -\mathbf{R}^{-1} \mathcal{A}_\mathbf{i}^T \mathbf{B}^T \mathbf{P}_\mathbf{i}, \tag{31}$$

while $\mathbf{P_i}$ is the positive-definite solution to the steady-state Riccati equation

$$\mathbf{Z} + \mathbf{P_i A} + \mathbf{A}^T \mathbf{P_i} - R_i \mathbf{P_i B} \mathcal{A}_\mathbf{i} \mathcal{A}_\mathbf{i}^T \mathbf{B}^T \mathbf{P_i} = 0. \tag{32}$$

6 Numerical study and discussion

The geometric specifications of the rotary thin-walled structure used in numerical study are shown in Table. 1. The material properties of host structure and piezo-actuators are specified in Tables 1 and 2, respectively. The corresponding CUS lay-up configurations are given in Table 3. Note that, validations of the present thin-walled beam model was performed in Refs.[23;24].

In this numerical study, unless otherwise stated, the following assumptions are adopted, (1) $\gamma_0 = -\beta_0$ is assumed in Eq. 2 to make the pretwist angle at the beam tip equal to zero; (2) the piezo-actuators are assumed spread over the entire beam span and bonded outside the host structure; (3) radius of the hub is assumed as $R_0 = 0.1L$; (4) the constant rotating speed is assumed as $\Omega = 1000\,\mathrm{rpm}$.

Table 1: Material properties (Graphite-Epoxy) and geometric specifications of the thin-walled box beam

Material	**Value**	**Geometric**	**Value**
E_{11}	$206.8 \times 10^9\ \mathrm{N/m^2}$	Width ($2b^a$)	0.254 m
$E_{22} = E_{33}$	$5.17 \times 10^9\ \mathrm{N/m^2}$	Depth ($2d^a$)	0.0681 m
$G_{12} = G_{13}$	$2.55 \times 10^9\ \mathrm{N/m^2}$	Hub radius (R_0)	0.2032 m
G_{23}	$3.10 \times 10^9\ \mathrm{N/m^2}$	Number of layers (N_h)	6
$\mu_{12} = \mu_{13} = \mu_{23}$	0.25	Layer thickness	0.0017 m
ρ	$1.528 \times 10^3\ \mathrm{Kg/m^3}$	Length (L)	2.032 m

[a] The length is measured on the mid-line contour.

Table 2: Material properties of piezo-actuator manufactured by MFC[35]

E_{11}	$31.2.8 \times 10^9\ \mathrm{N \cdot m^{-2}}$	d_{11}	$386.63 \times 10^{-12}\ \mathrm{m \cdot V^{-1}}$
$E_{22} = E_{33}{}^*$	$17.05 \times 10^9\ \mathrm{N \cdot m^{-2}}$	$d_{12} = d_{13}{}^*$	$-175.50 \times 10^{-12}\ \mathrm{m \cdot V^{-1}}$
$G_{12} = G_{13}{}^* = G_{23}{}^*$	$5.12 \times 10^9\ \mathrm{N \cdot m^{-2}}$	ρ	$5115.9\ \mathrm{Kg \cdot m^{-3}}$
$\mu_{12} = \mu_{13}{}^* = \mu_{23}{}^*$	0.303	m_p	1
Electrode spacing	0.0017 m	Thickness	0.0017 m

* The value is assumed by the author.

Table 3: CUS lay-up configurations (deg) [a]

		Flanges		Webs	
Layer	Material	Top	Bottom	Left	Right
CUS (1-6)	Host structure	$[\theta_h]_6$	$[\theta_h]_6$	$[\theta_h]_6$	$[\theta_h]_6$
CUS (7)	Piezo-actuator	$[\theta_p^F]$	$[\theta_p^F]$	$[\theta_p^W]$	$[\theta_p^W]$

[a] θ_h, θ_p^F and θ_p^W denote the ply-angles in host structure, flange-actuator-pair and web-actuator-pair, respectively. θ_p denotes both for θ_p^F and θ_p^W.

6.1 Study of piezo-actuator coefficients

The piezo-actuator coefficients induced by flange-actuator-pair (V_1) and web-actuator-pair (V_3) plotted as a function of ply-angle are illustrated in Figs. 4, 5 and Figs. 6, 7, respectively. The influences of host structure stiffness on piezo-actuator coefficients are also highlighted in these figures. For an unpretwisted rotary thin-walled beam, $\theta_h = 75^o, 105^o$ will yield a significant chordwise bending-flawise bending elastic coupling, while this elastic coupling is immaterial for $\theta_h = 90^o$ case[24].

It can be found that transverse shear coefficients $\mathcal{A}_1^{Qx}$ in Fig. 4 and $\mathcal{A}_3^{Qz}$ in Fig. 6 show a symmetric dependence centered around $\theta_p = 90^o$, while bending coefficients $\mathcal{A}_1^{Mx}$ in Fig. 5 and $\mathcal{A}_3^{Mz}$ in Fig. 7 present the anti-symmetric property. 5

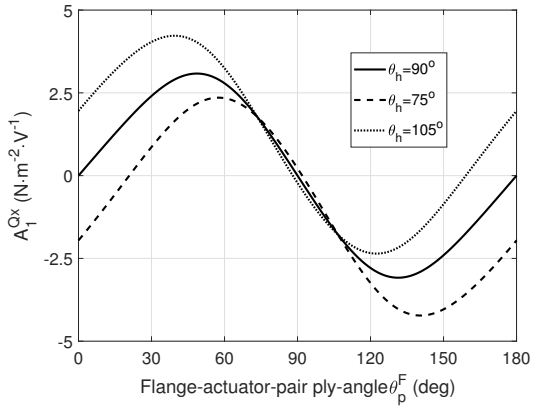

Figure 4: Chordwise transverse shear piezoelectric coefficient $\mathcal{A}_1^{Qx}$ as a function of flange-actuator-pair ply-angle θ_p^F.

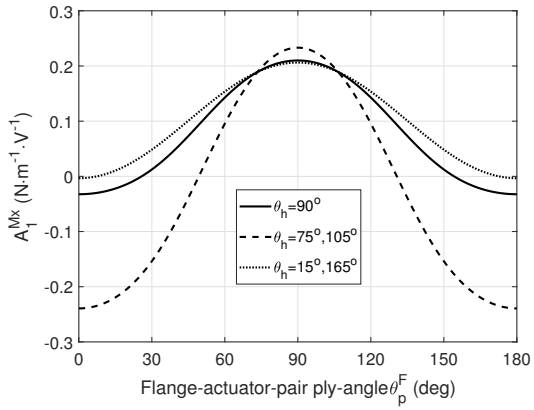

Figure 5: Flapwise bending piezoelectric coefficient $\mathcal{A}_1^{Mx}$ as a function of flange-actuator-pair ply-angle θ_p^F.

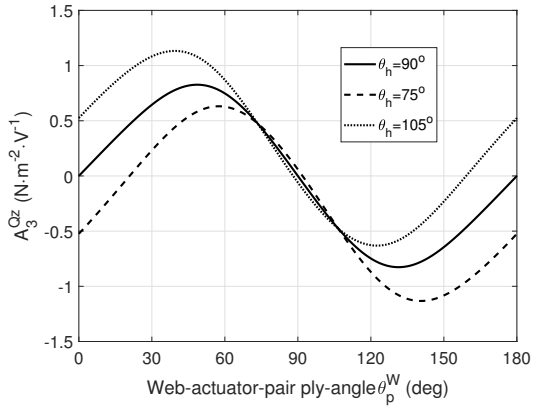

Figure 6: Flapwise transverse shear piezoelectric coefficient $\mathcal{A}_3^{Qz}$ as a function of web-actuator-pair ply-angle θ_p^W.

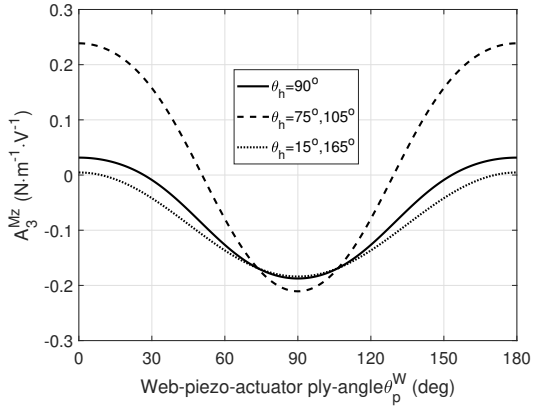

Figure 7: Chordwise bending piezoelectric coefficient $\mathcal{A}_3^{Qz}$ as a function of web-actuator-pair ply-angle θ_p^W.

6.2 Study of damping ratios

Recalling the LQR control methodology, the control authority is solely related to control weighing factor η_i. Figs. 8 and 9 plot damping ratios of the first four modes as a function of η_i. It can be found damping ratios decrease with the increase of η_i.

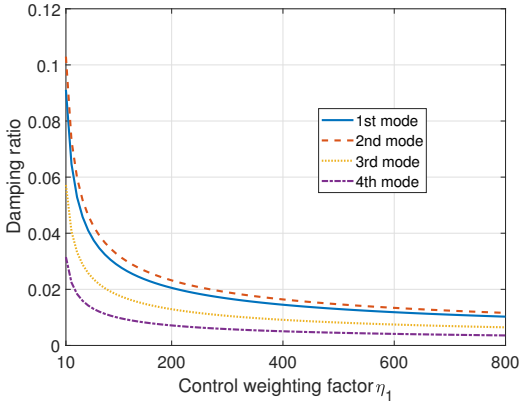

Figure 8: Damping ratios of the first four modes versus control weighting factor η_1; $\beta_0 = 0^o$, $\theta_h = 90^o$, $\theta_p^F = 80^o$

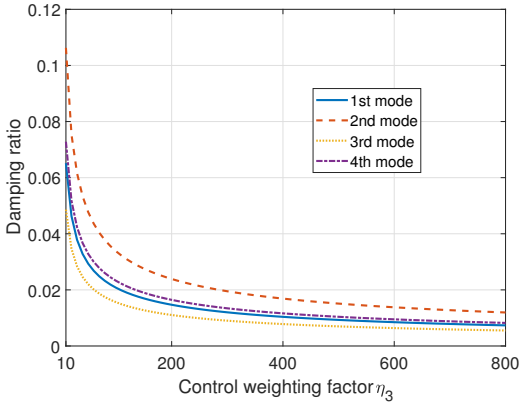

Figure 9: Damping ratios of the first four modes versus control weighting factor η_3; $\beta_0 = 0^o$, $\theta_h = 90^o$, $\theta_p^F = 80^o$

For $\theta_h = 90^o$ case that the flapwise bending and chordwise bending are elastically decoupled, damping ratios of the first four modes plotted as a function of ply-angle are shown in Figs. 10 and 11. In addition, the non-shear-actuation and non-bending-actuation points are indicated by black and red dots, respectively. According to mode shapes study, the 1st and 3rd are flapwise bending modes, while the 2nd and 4th are chordwise bending modes. The result of Fig. 10 presents that flange-actuator-pair can control chordwise bending modes by piezoelectrically induced chordwise transverse shear $\mathcal{A}_1^{Qx}$ while control flapwise bending modes by $\mathcal{A}_1^{Mx}$. Note that, $\mathcal{A}_1^{Qx}$ will offer a robust control authority on chordwise bending modes in the domain $10^o < \theta_p^F < 70^o$ or $110^o < \theta_p^F < 170^o$. Similar results can also be concluded for web-actuator-pair in Fig. 11.

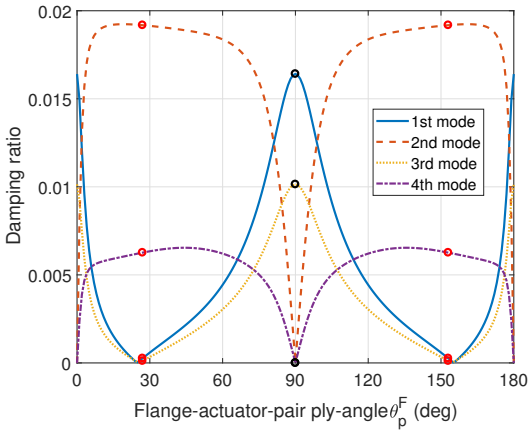

Figure 10: Damping ratios of the first four modess versus flange-actuator-pair ply-angle θ_p^F; $\theta_h = 90^o$, $\eta_1 = \eta_3 = 600$, $\beta_0 = 0^o$

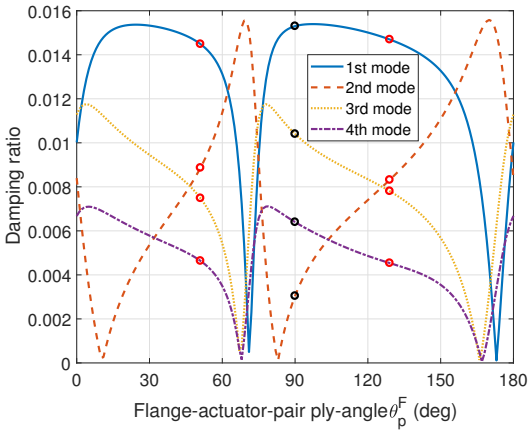

Figure 12: Damping ratios of the first four modess versus flange-actuator-pair ply-angle θ_p^F; $\theta_h = 75^o$, $\eta_1 = \eta_3 = 600$, $\beta_0 = 0^o$

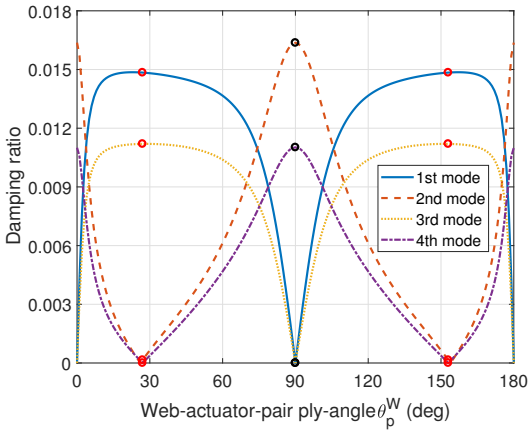

Figure 11: Damping ratios of the first four modes versus web-actuator-pair ply-angle θ_p^W; $\theta_h = 90^o$, $\eta_1 = \eta_3 = 600$, $\beta_0 = 0^o$

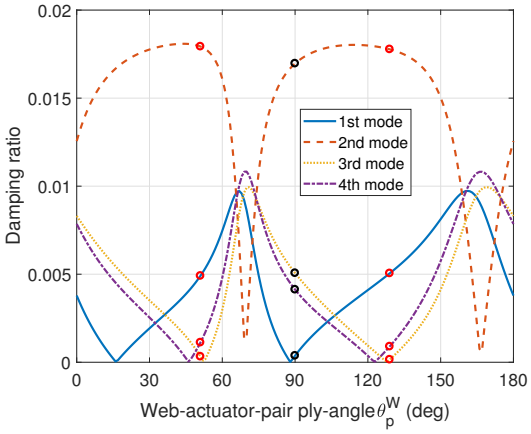

Figure 13: Damping ratios of the first four modes versus web-actuator-pair ply-angle θ_p^W; $\theta_h = 75^o$, $\eta_1 = \eta_3 = 600$, $\beta_0 = 0^o$

For the strong elastic couping case $\theta_p = 75^o$, Figs. 12 and 13 plot damping ratios of the first four modes as a function of flange-actuator-pair ply-angle θ_p^F and web-actuator-pair ply-angel θ_F^W, respectively. It can be found that the variations of damping ratios are complicated in Figs. 12 and 13. In Fig. 12, the flange-actuator-pair induced transverse shear force (indicated in red dots) or bending moment (indicated in black dots) can both control the flapwise and chordwise bending modes individually via elastic coupling. However in Fig. 13, the influence of elastic coupling on web-actuator-pair control effect is not as significant as on that of flange-actuator-pair. In general, in the domain of $60^o < \theta_p < 90^o$, the damping ratios vary sharply, while the variations are relatively slow in the domain of $90^o < \theta_p < 150^o$. We denote the last domain as the robust ply-angle domain.

Due to the pretwist angle, the chordwise and flapwise bending modes of the system will be always coupled each other. Figs. 14 and 15 present damping ratios of a pretwisted rotary thin-walled beam. Compared Fig. 14 with 12, the variations of damping ratios induced by flange-actuator-pair show the similarity. The significant influence of pretwisted angle can be seen on the 2nd mode which is indicated by dashed line. The variation similarity of damping ratios induced by web-actuator-pair can also be found in Figs. 15 and 13. The significant influence of pretwist angle can be observed on the 3rd and 4th modes.

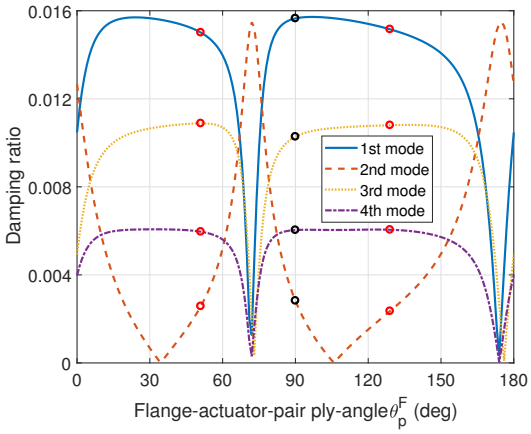

Figure 14: Damping ratios of the first four modess versus flange-actuator-pair ply-angle θ_p^F; $\theta_h = 75^o$, $\eta_1 = \eta_3 = 600$, $\beta_0 = 45^o$

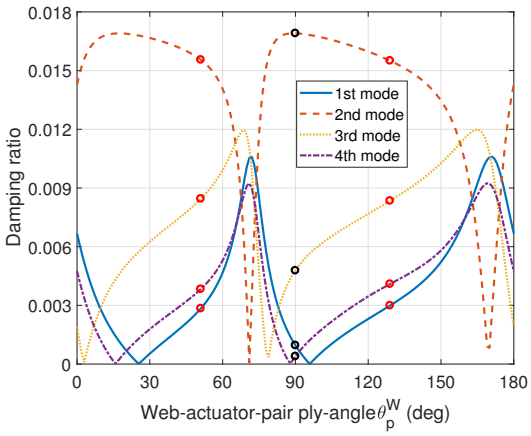

Figure 15: Damping ratios of the first four modes versus web-actuator-pair ply-angle θ_p^W; $\theta_h = 75^o$, $\eta_1 = \eta_3 = 600$, $\beta_0 = 45^o$

Figures 16-19 further highlight influence of pretwist angle on damping ratios induced by pure piezoelectric bending moment ($\theta_p = 90^o$) and transverse shear force ($\theta_p = 129^o$).

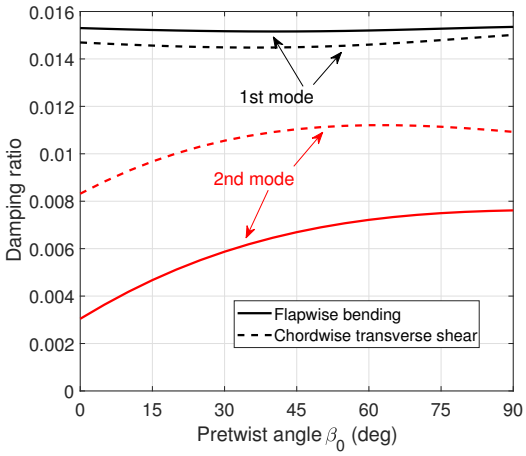

Figure 16: Damping ratios of 1st and 2nd modes versus pretwist angle β_0; $\theta_h = 75^o$, $\eta_1 = \eta_3 = 600$, $\theta_p^F = 90^o$ for flapwise bending, $\theta_p^F = 129^o$ for chordwise transverse shear

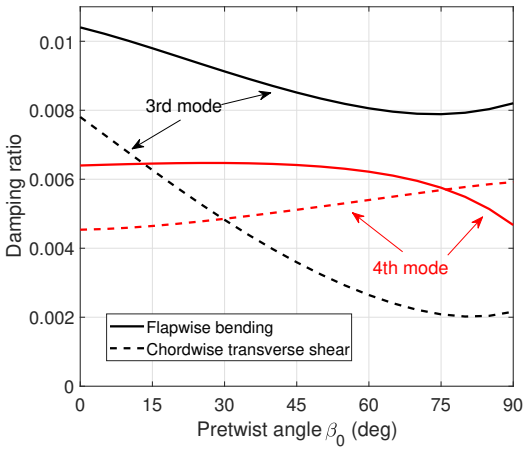

Figure 17: Damping ratios of 3rd and 4th modes versus pretwist angle β_0; $\theta_h = 75^o$, $\eta_1 = \eta_3 = 600$, $\theta_p^F = 90^o$ for flapwise bending, $\theta_p^F = 129^o$ for chordwise transverse shear

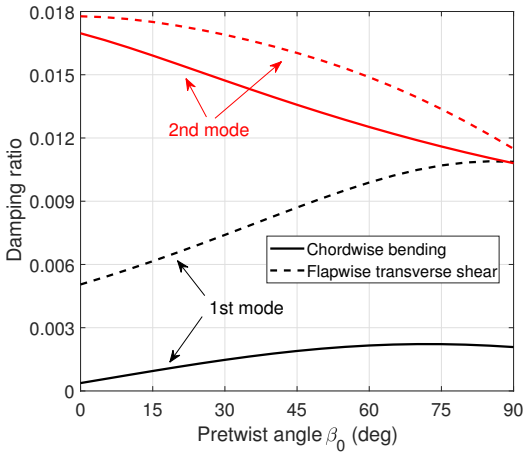

Figure 18: Damping ratios of 1st and 2nd modes versus pretwist angle β_0; $\theta_h = 75^o$, $\eta_1 = \eta_3 = 600$, $\theta_p^W = 90^o$ for chrodwise bending, $\theta_p^W = 129^o$ for flapwise transverse shear

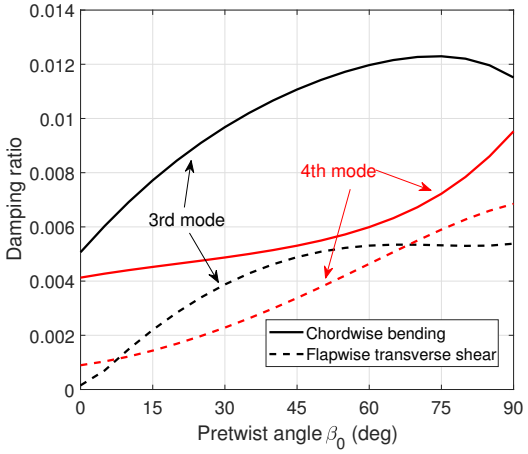

Figure 19: Damping ratios of 3rd and 4th modes versus pretwist angle β_0; $\theta_h = 75^o$, $\eta_1 = \eta_3 = 600$, $\theta_p^W = 90^o$ for chordwise bending, $\theta_p^W = 129^o$ for flapwise transverse shear

6.3 Dynamical simulation

A pretwisted rotary blade with strong elastic couplings is considered in this dynamic simulation. Piezo-actuator with $\theta_p = 135^o$ is implemented for the reason that on one hand this ply-angle is in the robust ply-angle domain, on the other hand it can yield a significant piezoelectrically induced torque on twist motion. Note that in the actual simulations, the first seven structural modes are used. The dynamic responses of the blade tip under the impulse load are presented in Fig.s 20 and 21. The associate voltage parameters are shown in Fig. 22. In order to make the output value of voltage V_1 and V_3 at the same level (see Fig. 22), the control weighting factors $\eta_1 = 600$ and $\eta_3 = 24000$ are adopted. It can be found that flange-actuator-pair present significant better control effect than that of web-actuator-pair no matter on lateral or vertical directions.

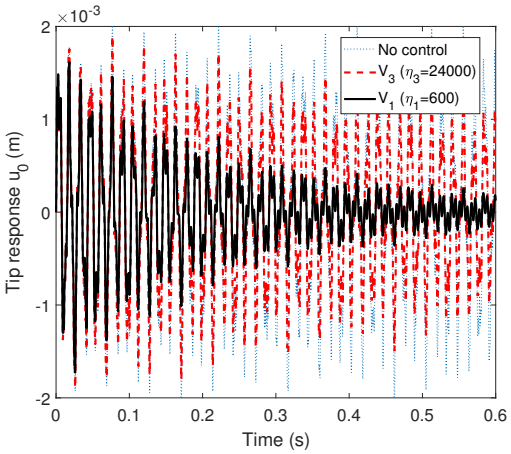

Figure 20: Beam tip response on lateral direction $u_0(L,t)$ to impulse load; $p_x = p_z = 10\,\mathrm{N{\cdot}m^{-1}}$, $\theta_h = 75^o$, $\theta_p = 135^o$, $\beta_0 = 60^o$.

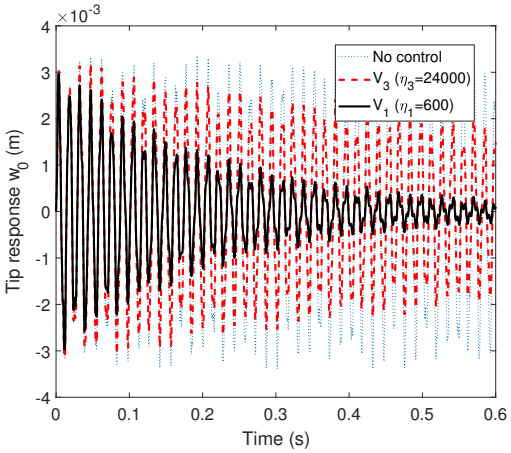

Figure 21: Beam tip response on vertical direction $w_0(L,t)$ to impulse load; $p_x = p_z = 10\,\mathrm{N{\cdot}m^{-1}}$, $\theta_h = 75^o$, $\theta_p = 135^o$, $\beta_0 = 60^o$.

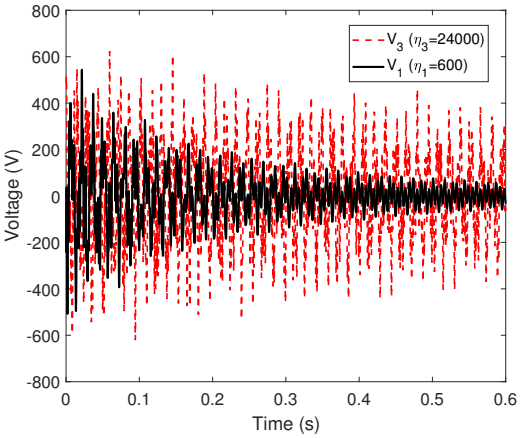

Figure 22: Time history of voltages to impulse load; $p_x = p_z = 10\,\mathrm{N{\cdot}m^{-1}}$, $\theta_h = 75^o$, $\theta_p = 135^o$, $\beta_0 = 60^o$.

7 Conclusions

A dynamic theory of pretwist rotating blades modeled as thin-walled beams incorporating fiber-reinforced and piezo-composite materials obtained via Hamiltons variational principle was supplied. The theory accounts for a number of nonclassical features such as transverse shear, warping inhibitions and centrifugal stiffening that are essential for a reliable prediction of dynamic characteristics. The piezo-actuators are grouped as two independent actuator-pairs, viz., flange-actuator-pair and web-actuator-pair. Based on the LQR control strategy, the strong and synergistic effect played by the directionality property of piezo-composite materials, considered in conjunction with that of tailored fiber-reinforced host structure, on their dynamic response characteristics was highlighted. Major conclusions include:

1. the stiffness of host structure has a significant effect on piezo-actuator coefficients;

2. pretiwst angle affects the control authority significantly;

3. flange-actuator-pair presents a much better control performance on vibration suppression than that of web-actuator-pair.

References

[1] Dewey H Hodges. Review of composite rotor blade modeling. *AIAA journal*, 28(3):561–565, 1990.

[2] Omri Rand. Analysis of composite rotor blades. In *Numerical Analysis and Modelling of Composite Materials*, pages 1–26. Springer, 1996.

[3] Sung Nam Jung, VT Nagaraj, and Inderjit Chopra. Refined structural dynamics model for composite rotor blades. *AIAA journal*, 39(2):339–348, 2001.

[4] Erasmo Carrera, Matteo Filippi, and Enrico Zappino. Free vibration analysis of rotating composite blades via carrera unified formulation. *Composite Structures*, 106:317–325, 2013.

[5] F. Demoures, F. Gay-Balmaz, S. Leyendecker, S. Ober-Blöbaum, T. S. Ratiu, and Y. Weinand. Discrete variational lie group formulation of geometrically exact beam dynamics. *Numerische Mathematik*, 130(1):73–123, 2015.

[6] Lawrence W Rehfield, Ali R Atilgan, and Dewey H Hodges. Nonclassical behavior of thin-walled composite beams with closed cross sections. *Journal of the American Helicopter Society*, 35(2):42–50, 1990.

[7] Ramesh Chandra and Inderjit Chopra. Experimental-theoretical investigation of the vibration characteristics of rotating composite box beams. *Journal of Aircraft*, 29(4):657–664, 1992.

[8] O Song and L Librescu. Structural modeling and free vibration analysis of rotating composite thin-walled beams. *Journal of the American Helicopter Society*, 42(4):358–369, 1997.

[9] O Song, N-H Jeong, and L Librescu. Vibration and stability of pretwisted spinning thin-walled composite beams featuring bending–bending elastic coupling. *Journal of Sound and Vibration*, 237(3):513–533, 2000.

[10] S-Y Oh, O Song, and L Librescu. Effects of pretwist and presetting on coupled bending vibrations of rotating thin-walled composite beams. *Int. J. Solids Struct.*, 40(5):1203–1224, 2003.

[11] S-Y Oh, L Librescu, and O Song. Modelling and vibration of composite thin-walled rotating blades featuring extension-twist elastic coupling. *Aeronautical Journal*, 109(1095):233–246, 2005.

[12] Gian Luca Ghiringhelli, Pierangelo Masarati, Marco Morandini, and Davide Muffo. Integrated aeroservoelastic analysis of induced strain rotor blades. *Mechanics of Advanced Materials and Structures*, 15(3-4):291–306, 2008.

[13] Claudio Brillante, Marco Morandini, and Paolo Mantegazza. Periodic controllers for vibration reduction using actively twisted blades. *The Aeronautical Journal*, 120(1233):1763–1784, November 2016.

[14] S Glukhikh, E Barkanov, A Kovalev, Pierangelo Masarati, Marco Morandini, Johannes Riemenschneider, and Peter Wierach. Design of helicopter rotor blades with actuators made of a piezomacrofiber composite. *Mechanics of Composite Materials*, 44(1):57–64, 2008.

[15] Pierangelo Masarati and Gian Luca Ghiringhelli. Characterization of anisotropic, non-homogeneous plates with piezoelectric inclusions. *Computers & Structures*, 83(15-16):1171–1190, June 2005.

[16] Liviu Librescu and Sung Soo Na. Dynamic response of cantilevered thin-walled beams to blast and sonic-boom loadings. *Shock and Vibration*, 5(1):23–33, 1998.

[17] Sungsoo Na and Liviu Librescu. Oscillation control of cantilevers via smart materials technology and optimal feedback control: actuator location and power consumption issues. *Smart Materials and Structures*, 7(6):833, 1998.

[18] Sungsoo Na, Liviu Librescu, Myung-Hyun Kim, In-Joo Jeong, and Pier Marzocca. Robust aeroelastic control of flapped wing systems using a sliding mode observer. *Aerosp. Sci. Technol.*, 10(2):120–126, 2006.

[19] Seung-Chan Choi, Jae-Sang Park, and Ji-Hwan Kim. Vibration control of pre-twisted rotating composite thin-walled beams with piezoelectric fiber composites. *J. Sound Vib.*, 300(1):176–196, 2007.

[20] Liviu Librescu, Sungsoo Na, Zhanming Qin, and Bokhee Lee. Active aeroelastic control of aircraft composite wings impacted by explosive blasts. *J. Sound Vib.*, 318(1):74–92, 2008.

[21] Seok-Ju Cha, Ji-Seok Song, Hwan-Hee Lee, Sungsoo Na, Jae-Hong Shim, and Piergiovanni Marzocca. Dynamic response control of rotating thin-walled composite blade exposed to external excitations. *J. Aerosp. Eng.*, 27(5):04014025, 2014.

[22] Ohseop Song, Liviu Librescu, and Sang-Yong Oh. Vibration of pretwisted adaptive rotating blades modeled as anisotropic thin-walled beams. *AIAA journal*, 39(2):285–295, 2001.

[23] Xiao Wang, Marco Morandini, and Pierangelo Masarati. Velocity feedback damping of piezo-actuated wings. *Composite Structures*, 174:221 – 232, 2017.

[24] Xiao Wang, Marco Morandini, and Pierangelo Masarati. Modeling and control for rotating pretwisted thin-walled beams with piezo-composite. *Composite Structures*, 180:647 – 663, 2017.

[25] Xiao Wang and Zhanming Qin. Nonlinear modal interactions in composite thin-walled beam structures with simultaneous 1:2 internal and 1:1 external resonances. *Nonlinear Dynamics*, 86(2):1381–1405, 2016.

[26] RE Kielb. Effects of warping and pretwist on torsional vibration of rotating beams. *Journal of applied mechanics*, 51:913, 1984.

[27] Aaron Alton Bent. *Active fiber composites for structural actuation*. PhD thesis, Massachusetts Institute of Technology, 1997.

[28] William K Wilkie, Robert G Bryant, James W High, Robert L Fox, Richard F Hellbaum, Anthony Jalink Jr, Bruce D Little, and Paul H Mirick. Low-cost piezocomposite actuator for structural control applications. In *SPIE's 7th Annual International Symposium on Smart Structures and Materials*, pages 323–334. International Society for Optics and Photonics, 2000.

[29] L. Librescu and O. Song. *Thin-Walled Composite Beams: Theory and Application*. Springer, New York, 2006. Chap.8, pp. 213-232.

[30] Lawrence W Rehfield and Ali R Atilgan. Toward understanding the tailoring mechanisms for thin-walled composite tubular beams. In *Proceedings of the First USSR-US Symposium on Mechanics of Composite Materials, Riga, Latvia, May*, pages 23–26, 1989.

[31] L. Librescu and S.S. Na. Dyanmic response of cantilevered thin-wlled beams to blast and sonic-boom loadings. *Shock. Vib.*, 5(1):23–33, 1998.

[32] A.N. Palazotto and P.E. Linnemann. Vibration and buckling characteristics of com-posite cylindrical panels incorporating the effects of a higher order shear theory. *Int. J. Solids Struct.*, 28(3):341–361, 1991.

[33] L Librescu, L Meirovitch, and Sung Soo Na. Control of cantilever vibration via structural tailoring and adaptive materials. *AIAA journal*, 35(8):1309–1315, 1997.

[34] W Keith Belvin and KC Park. Structural tailoring and feedback control synthesis-an interdisciplinary approach. *Journal of Guidance, Control, and Dynamics*, 13(3):424–429, 1990.

[35] Jae-Sang Park and Ji-Hwan Kim. Analytical development of single crystal macro fiber composite actuators for active twist rotor blades. *Smart Mater. Struct.*, 14(4):745, 2005.